Journal of
Materials Chemistry C

Materials for optical, magnetic and electronic devices

Accepted Manuscript

This article can be cited before page numbers have been issued, to do this please use: H. B. Cho, J. Y. Moon, J. W. Min, H. J. Kim, H. U. Lee, H. P. Park, S. W. Jang, J. M. Seo, S. B. Cho, H. Yang and W. B. Im, *J. Mater. Chem. C*, 2025, DOI: 10.1039/D5TC02166A.

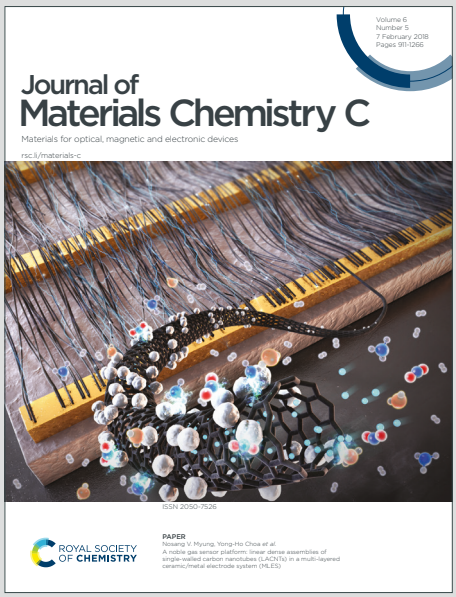

ROYAL SOCIETY OF CHEMISTRY

rsc.li/materials-c

View Article Online
DOI: 10.1039/D5TC02166A

Phosphotungstic and phosphomolybdic acid solid-solutions: a new approach for QLED hole injection layers†

Han Bin Cho,‡[a] Ji Yoon Moon,‡[a] Jeong Wan Min,‡[a] Ha Jun Kim,‡[a] Han Uk Lee,[c] Hwa Pyeong Park,[a] Sung Woo Jang,[a] Jeong Min Seo,[a] Sung Beom Cho,[b,c] Heesun Yang,[d]* and Won Bin Im[a]*

[a]*Division of Materials Science and Engineering, Hanyang University, 222 Wangsimni-ro, Seongdong-gu, Seoul, 04763, Republic of Korea*

[b]*Department of Materials Science and Engineering, Ajou University, Suwon, Gyeonggi-do 16499, Republic of Korea*

[c]*Department of Energy Systems Research, Ajou University, Suwon, Gyeonggi-do 16499, Republic of Korea*

[d]*Department of Materials Science and Engineering, Hongik University, Seoul 04066, Republic of Korea*

Corresponding Authors E-mail: hyang@hongik.ac.kr and imwonbin@hanyang.ac.kr

‡These authors contributed equally to this work

†Supplementary Information available

View Article Online
DOI: 10.1039/D5TC02166A

Abstract

The organic hole injection layer (HIL) PEDOT:PSS used in QLEDs has issues with bottom electrode corrosion and charge imbalance with electrons. To address these issues, we developed a solid-solution inorganic hole injection layer by alloying the phosphomolybdic acid (PMA), which has high charge mobility, and phosphotungstic acid (PWA), which has high stability. By varying the W-Mo ratio, we could adjust the energy band alignment of the hole injection layer. As a result, the efficiency of the device was improved by preventing hole accumulation caused by the large energy barrier at the interfaces in the HIL when holes are injected from the ITO electrode. By adjusting the Mo ratio in PWA-PMA, the conductivity of the hole injection layer can be easily tuned. The enhanced hole mobility resolved the charge imbalance issue, leading to higher device efficiency and a reduction in turn-on voltage. This work enables the use of PWA-PMA as a hole-injection layer in QLEDs for the first time.

View Article Online
DOI: 10.1039/D5TC02166A

1. Introduction

Quantum dot light-emitting diodes (QLEDs) utilizing colloidal quantum dots (QDs) have emerged as front-runners in future display technology. QLEDs exhibit various advantageous features such as diverse color selection, superior efficiency, low power consumption, cost-effectiveness, and compatibility with large flexible substrates.[1–4] The QLED technology has seen significant advancements, demonstrating high luminous efficiency and external quantum efficiencies (EQEs) exceeding 20%, rivaling those of OLEDs.[5,6] In recent years, the performance of QLED devices has markedly improved alongside the development of QLED components. However, the acidity of the organic hole injection layer, predominantly utilizing PEDOT:PSS, in typical QLEDs leads to degradation of the underlying electrode layer ITO, compromising long-term operational stability. Additionally, the slower mobility of organic hole transport materials compared to inorganic electron transport materials can result in charge imbalance issues. To address these stability and charge imbalance concerns, various inorganic materials such as MoO_3, NiO_x, V_2O_5, and VO_2 have been introduced.[7–10] Inorganic materials have inherent valence band maximum (VBM) and conduction band minimum (CBM). Therefore, there are limitations in tuning the energy band alignment of HIL when used with various types of hole transport layers.

Recently, typical metal oxide clusters with a size of 1 nanometer, known as polyoxometalates (POM), have been utilized as charge transport materials in various optoelectronic devices due to their excellent solubility, well-defined morphology, high transparency in the visible spectrum, and highly tunable structural characteristics.[11] Particularly, phosphomolybdic acid ($H_3PMo_{12}O_{40}$, PMA), which contains MoO_3, is a typical POM with a Keggin structure and is sensitive to electron transfer. PMA has been investigated as an effective hole transport material in solar cells, QLEDs, and OLEDs owing to its excellent electron-

View Article Online
DOI: 10.1039/D5TC02166A

accepting capability and low operating function.[12] In addition, phosphotungstic acid ($H_3PW_{12}O_{40}$, PWA) shares the same crystal structure and possesses high chemical and thermal stability, making it a versatile charge transport material in various optoelectronic devices.[13–15] However, PWA alone exhibits significant band offset and relatively lower charge mobility compared to PMA for charge injection. To address this limitation, Fan Cao et al. doped Cl, Cu, and other elements into PWA as a charge injection layer to adjust the energy level alignment and enhance charge mobility, thereby improving hole mobility and ultimately achieving higher efficiency QLEDs.[15,16]

In this study, we developed a hole injection layer (HIL) for QLEDs with high charge mobility and stability by solid-solution of PMA, known for its high charge mobility, and PWA, known for its high stability. We used the sol-gel method to fabricate PWA-PMA solid-solution thin films. Additionally, PWA-PMA thin films, as a HIL with various energy band alignments, were applied to QLEDs. In-depth crystallographic analysis was conducted to examine the phase transition regions of PWA-PMA, and computational science was employed to verify the electrical properties. Moreover, electron leakage current was prevented, and charge balance was improved by increasing conductivity and carrier mobility due to the use of the solid-solution. As a result, a decrease in the turn-on voltage was observed, and high EQE was achieved through effective hole injection. The enhanced conductivity of the PWA-PMA thin films successfully alleviated the interfacial resistance of the device, promoting efficient hole injection. Additionally, the improved hole mobility addressed charge imbalance, resulting in increased device efficiency. The turn-on voltage of the QLED decreased, and a high EQE was achieved through effective hole injection.

View Article Online
DOI: 10.1039/D5TC02166A

2. Results and discussion

The synthesized $PW_{12}O_{40}$-$PMo_{12}O_{40}$ (PWA-PMA) thin film was prepared through annealing at 250℃ under ambient conditions. **Fig. 1a** shows the XRD patterns of the $PW_{12-12x}Mo_{12x}O_{40}$ series (PWA: $PW_{12}O_{40}$, W09: $PW_{10.8}Mo_{1.2}O_{40}$, W07: $PW_{8.4}Mo_{3.6}O_{40}$, W05: $PW_6Mo_6O_{40}$, W03: $PW_{3.6}Mo_{8.4}O_{40}$, W01: $PW_{1.2}Mo_{10.8}O_{40}$, PMA: $PMo_{12}O_{40}$). PWA ($Fd\bar{3}m$) and PMA ($Pn\bar{3}m$) exhibit a Keggin structure, where a tetrahedron composed of central P atoms is linked to 12 neighboring octahedral MoO_6 or WO_6 units *via* oxygen atoms, confined within a cage. In the octahedra formed by W and O, the bond length of W-O bonds is 1.72 Å, while in the tetrahedra composed of P and O, the W-O bond length connected to O is 2.51 Å. On the other hand, in the octahedra formed by Mo and O, the bond length of Mo-O bonds is 1.70 Å, and the P-O bond length connected to O is 2.50 Å. In **Fig. 1b**, it is evident that both materials have the same Keggin structure and chemical formula. The distances between W-O and Mo-O in each octahedron are nearly identical, and the P-O bond length in the tetrahedra is consistent, facilitating solid-solution formation. As the Mo substitution concentration increases in PWA, maintaining the $Fd\bar{3}m$ structure up to W05, a structural transition to $Pn\bar{3}m$ occurs from W03 onward during the progression of the solid-solution (**Fig. S2**). Specifically, up to $PW_{4.2}Mo_{7.8}O_{40}$, the $Fd\bar{3}m$ structure is retained, but starting from W03 ($PW_{3.6}Mo_{8.4}O_{40}$), a phase transition to the $Pn\bar{3}m$ structure is observed.

Furthermore, the mixing behavior of PWA-PMA solid-solutions was theoretically investigated using density functional theory (DFT) at various temperatures. As shown in **Fig. 1c**, the Gibbs free energies of mixing were calculated as a function of W concentration. It was found that the PWA phase can be stabilized from W03 at the synthesis temperature (250°C), as well as at room temperature (25°C) and the maximum operating device temperature (80°C). Through this, it was confirmed that experimental and theoretical results precisely matched. The

View Article Online
DOI: 10.1039/D5TC02166A

similar ionic radii of Mo^{6+} (0.59 Å) and W^{6+} (0.60 Å) result in minimal changes in the lattice parameters of the crystal structure with increasing Mo substitution concentration. Therefore, observing specific peak changes in XRD becomes challenging, making it difficult to precisely confirm the substitution of Mo.

To assess whether an effective substitution of Mo occurred to address this issue, FTIR analysis was conducted (**Fig. 1d**). The FTIR spectra of the PWA-PMA solid-solution were observed in the wavelength range of 1100-700 cm^{-1}. PWA exhibited stretching modes of vibration at 1080, 954, and 880 cm^{-1}, corresponding to P-O, W=O, and W-O-W, respectively. Conversely, PMA displayed stretching modes of vibration at 1064, 965, and 868 cm^{-1}, corresponding to P-O, Mo=O, and Mo-O-M, respectively. A shoulder peak in the P-O band began to emerge at W09 in PMA, and as the Mo substitution ratio increased, a gradual shift in the peak was observed. Additionally, peak shifts were observed at 860-880 cm^{-1}, corresponding to bonding with corner oxygen, with pronounced changes in peaks, particularly at W03 where phase transition occurs. These observations collectively suggest the occurrence of a complete solid-solution between PWA and PMA.

To investigate the subtle differences in structural disorder caused by the crystal structure, we calculated the Urbach energy (**Fig. S3**). Urbach energy is a dimension of energy used to measure the energetic disorder at the band edge of a semiconductor. This is obtained by fitting the absorption coefficient to an exponential function. Urbach energy, being influenced by the disorder in the crystal structure, is depicted as a function of Mo substitution concentration. From W05 to PWA, it can be observed that as the Mo substitution concentration increases, the Urbach energy also increases, indicating an increase in structural disorder. Conversely, from W03 to PMA, the Urbach energy decreases, suggesting a decrease in structural disorder as PMA is approached. It is anticipated that as the Urbach energy decreases,

View Article Online
DOI: 10.1039/D5TC02166A

the extent of electronic disorder decreases, resulting in a reduction in carrier trap states.

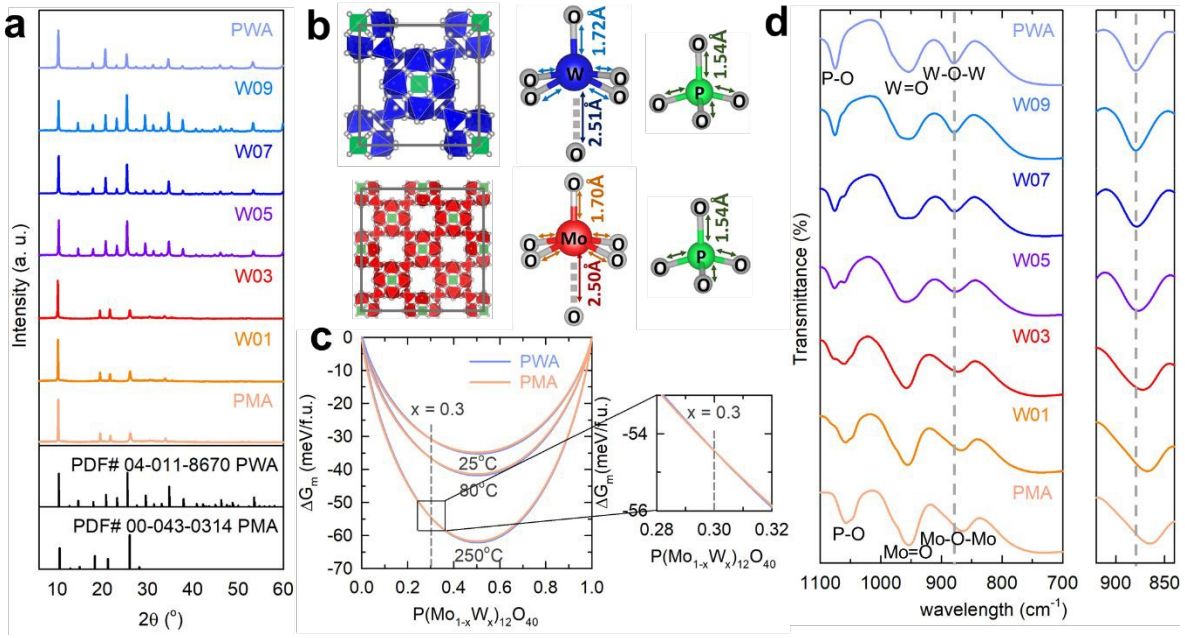

Fig. 1 (a) X-ray diffraction (XRD) patterns and (c) Gibbs free energy of mixing for $PW_{12}O_{40}$ (PWA)−$PW_{12}O_{40}$ (PMA) solid-solution series. (b) Crystal structure of PWA and PMA, where blue, red, green, and grey spheres represent the tungsten, molybdenum, phosphine, and oxygen atoms, respectively. Distinct crystallographic sites of W and Mo with sixfold coordination and P with fourfold coordination. (d) Fourier transform infrared (FTIR) of $PW_{12}O_{40}$ (PWA)−$PW_{12}O_{40}$ (PMA) solid-solution series.

To elucidate the effect of Mo mixing, the electronic and surface properties of PWA-PMA alloys were investigated. The electronic properties of solid-solutions were analyzed through density of states (DOS), as shown in **Fig. 2a**. It is well reported from previous calculations that the band gap of $PW_{12}O_{40}$ (PWA) is ~ 2.8 eV, while that of $PMo_{12}O_{40}$ (PMA) is ~ 2 eV and this qualitative trend is consistent with our calculated results.[17,18] Furthermore, following Vegard's law, the bandgap of heterostructural alloys is a function of the composition of their end-members.[19,20] Consequently, it is expected that the overall bandgap will decrease as the composition of PMA, which has a relatively smaller bandgap, increases. Indeed, our

View Article Online
DOI: 10.1039/D5TC02166A

calculations confirm this, demonstrating that the band gap decreases as the Mo composition increases (i.e., a reduction of W composition, **Fig. 2a**).

In **Fig. 2b**, the surface morphology of PWA and PMA films was examined using Scanning Electron Microscopy (SEM). This analysis offers insights into the morphological changes induced by molybdenum substitution in PWA. The PWA thin film displays a smooth surface with minimal crystalline features but with visible cracks. These cracks function as pinholes, adversely affecting the current leakage of the device. In contrast, the W09 film exhibits finer crystalline structures. This observation indicates that even a minor substitution of molybdenum can lead to significant differences in the thin film's surface. As the molybdenum content increases, the number of cracks decreases, and the film becomes more crystalline. Conversely, the PMA film shows no cracks and demonstrates the most uniform surface. To assess the surface roughness of each film, AFM analysis was performed, as shown in **Fig. 2c**. The PWA film had a surface roughness of 2.34 nm, while the W09 film exhibited a slight reduction to 2.20 nm. This reduction suggests that even a small amount of molybdenum substitution can result in a smoother film. The surface roughness decreases with increasing molybdenum content, suggesting the potential for producing more uniform films.

View Article Online
DOI: 10.1039/D5TC02166A

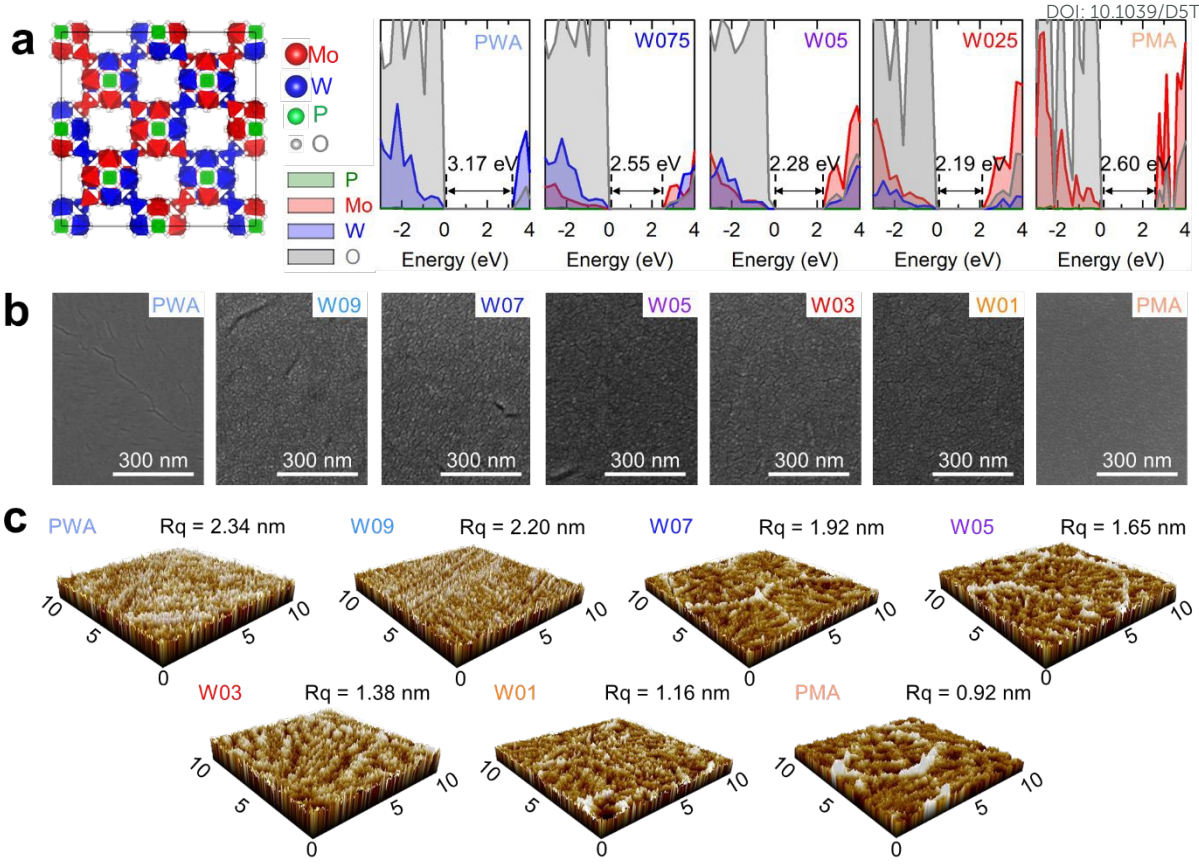

Fig. 2 (a) The atomic structure of PWA-PMA solid-solution, and the density of states as a function of W. (b) SEM images and (c) AFM images of PWA-PMA solid-solution films.

Fig. 3a shows the schematic of a QLED structure composed of ITO/PWA-PMA/TFB/InP QDs/ZMO/Al, with PWA-PMA as the charge injection layer. **Fig. 3b** shows the cross-sectional transmission electron microscopy (TEM) image of a 45 nm-thick QLED integrated with PWA-PMA, with individual layer thicknesses also indicated. Clear boundaries between TFB and PWA-PMA are observed in the energy-dispersive spectroscopy (EDS) compositional mapping image (**Fig. S4**). Upon analyzing the absorption spectra of the PWA-PMA series depicted in **Fig. S5**, the predominant absorption occurs within the 250 to 400 nm range. With increasing Mo content, absorption is observed in a broad range starting from 600 nm, attributed to oxygen vacancies resulting from the reduction of Mo^{6+}.[21] Upon observation

View Article Online
DOI: 10.1039/D5TC02166A

of the thin film and solution images of the PWA-PMA series in **Fig. S6**, it is noted that as the Mo content increases, the color of the solution shifts towards yellowish and the color of the thin film darkens. Consequently, analysis of the optical band gap of the PWA-PMA series using the Tauc plot indicates a sequential decrease in band gap as the Mo content increases (**Fig. 3c**). Nonetheless, despite these findings, examination of the thin film's transmittance reveals a high transmittance ranging from 89% to 98% at the luminescence maximum of Red InP QD, approximately 630 nm (**Fig. S7**). The electronic structures of PWA-PMA films were analyzed utilizing ultraviolet photoelectron spectroscopy (UPS). Fig. 3d displays the UPS spectra depicting both the secondary-electron cut-off region and the valence band edge region for the PWA-PMA films. Considering the Tauc plot and UPS data, the overall energy band alignment was illustrated in **Fig. 3e**. In PWA-W05 films with the same crystal structure, a trend was observed where the difference between E_F-$E_{VBM,HIL}$ values decreased as the proportion of Mo increased. A similar phenomenon was also observed in W03-PMA films. Particularly, when holes were injected into the device, difficulty in hole injection arose due to the large energy barrier difference in PWA, leading to hole accumulation. However, in W07 films, it can be inferred that the reduction in energy barrier difference facilitates sequential hole injection into TFB.

View Article Online
DOI: 10.1039/D5TC02166A

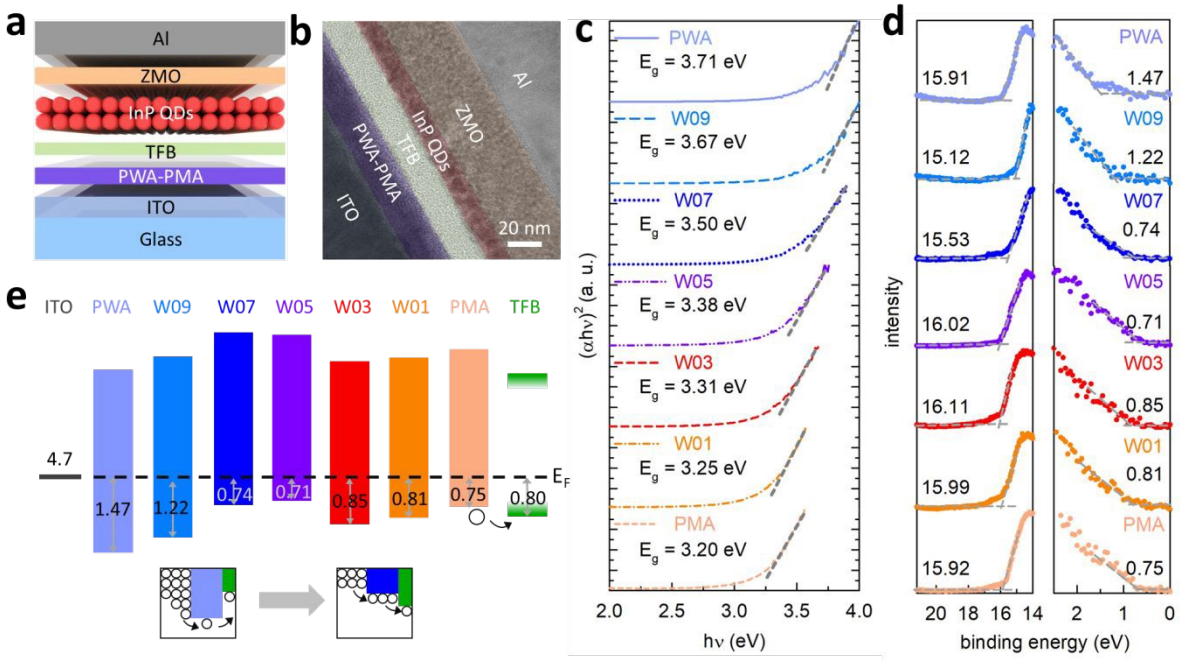

Fig. 3 (a) Illustration of QLED structure and (b) cross-sectional TEM images of the QLED using PWA-PMA solid-solution films as HIL. (c) Plots of $(\alpha h\upsilon)^2$ for the optical bandgap and (d) UPS spectra of valence-band edge region and secondary electron cut-off region for PWA-PMA solid-solution films. (e) Energy level alignment diagram for PWA-PMA solid-solution films/TFB.

In **Fig. 4a**, a slight red shift between the photoluminescence (PL) and electroluminescence (EL) spectra is observed, which is attributed to the Stark effect occurring when an external electric field is applied to densely packed quantum dots. In **Fig. 4b**, the conductivity of ITO and PWA-PMA thin films was examined by observing the I-V characteristics of PWA-PMA between ITO and Al. Conductivity can be calculated by multiplying the thickness of the PWA-PMA (20 nm) with the slope obtained from the J-V graph (**Fig. S8**). As a result, PWA showed the lowest conductivity at 4.59×10^{-5} S cm^{-1}, and as the ratio of Mo increased, the conductivity increased, reaching the highest value of 8.23×10^{-5} S cm^{-1} in PMA. Notably, there was a significant increase in conductivity between W05 and W07. To understand this, we calculated the effective mass of holes in the $Pn\bar{3}m$ structure

View Article Online
DOI: 10.1039/D5TC02166A

of PWA and the $Fd\bar{3}m$ structure of PMA using computational science. The effective mass of holes in PWA was 10.07, while in the $Fd\bar{3}m$ structure of PMA, it was 7.93. This indicates that as the ratio of Mo increases, the conductivity, which is inversely proportional to the effective mass, also increases. Specifically, there is a significant increase in conductivity at the phase transition point around W03. In **Fig. 4c**, a hole-only device (HOD) was fabricated, and the hole mobility was calculated using the space-charge limited current (SCLC) equation, with results summarized in **Table 1**. As the Mo content increased in PWA, which initially had low mobility, there was a gradual increase in mobility, reaching the highest in PMA. This suggests that substituting Mo in the stable PWA enhances hole mobility, improving charge balance with electrons and potentially increasing device efficiency.

The impact of using PWA-PMA as a hole injection layer on QLED performance was investigated. Additionally, the performance of the QLED is summarized in **Table 2**. **Fig. 4d** illustrates the current density-voltage characteristics of PWA-PMA QLEDs. At low voltages, PWA and PMA exhibit high current densities, while W09-W01 show significantly lower current density values by three orders of magnitude. This suggests electron leakage occurring in the pre-turn-on low-voltage region (<3V) for PWA and PMA. However, in the W09-W01 region, effective prevention of electron leakage is observed. In the post-turn-on high-voltage region, where current density is higher or comparable, it indicates more effective electron injection. Particularly, in W07, the lowest current density is observed before the turn-on voltage, while the highest current density is observed after turn-on, indicating its most effective operation. In **Fig. 4e**, it can be observed that efficiency roll-off occurs as the current density increases. This phenomenon is particularly pronounced in PWA and PMA. Efficiency roll-off is caused by electric field-induced photoluminescence quenching.[22] At high currents, it occurs as QDs become charged due to excess electrons, indicating a stronger charge imbalance in PWA and PMA. In contrast, devices using solid-solutions exhibit less efficiency roll-off,

View Article Online
DOI: 10.1039/D5TC02166A

suggesting improved charge balance. Notably, W07 shows the highest EQE value. In **Fig. 4f**, it was observed that the PMA with the highest carrier mobility and conductivity exhibited the lowest turn-on voltage. However, despite being composed entirely of Mo, PMA does not yield the most favorable EQE roll-off, which can be attributed to its limited carrier concentration. The hole injection rate is attributed to both the charge carrier mobility and carrier concentration of the charge transport layers (CTLs).[23] In our solid-solution system, these should be more precisely considered to achieve not only charge balance but also high EQE. In this perspective, a careful optimization of the trade-off between mobility and carrier concentration is essential to simultaneously achieve a good efficiency roll-off and high EQE in our system. Furthermore, we fabricated electron-only devices (EODs) to compare the current density gap with hole-only devices (HODs), as shown in **Fig. S9**. The optimized W07 composition exhibits a substantially smaller current density gap compared to pristine PWA, indicating improved charge balance. Interestingly, only PMA and W05–W07 exhibit notably low turn-on voltages, likely due to high mobility in PMA and enhanced charge balance in the W05–W07 region in **Fig. 4f**.

Although W05 offers one of the favorable energy level alignments with TFB, increased structural disorder may lead to higher electrical resistivity, compromising device efficiency. This is supported by the XRD patterns in **Fig. 1(a)**, as well as the Urbach energy values shown in **Fig. S3**. Notably, W05 is the first composition in the series where both PWA and PMA diffraction features simultaneously appear, and it also exhibits high Urbach energies among the series, indicating increased disorder. These structural characteristics appear to impact charge transport properties.

Furthermore, we evaluated the operational stability of QLED devices with identical structure but different hole injection layers, as shown in **Fig. S10**. The device incorporating PMA exhibited relatively poor stability under ambient conditions, with a T_{50} (time to 50% of

View Article Online
DOI: 10.1039/D5TC02166A

the initial luminance at 900 cd/m^2) of only about 11 hours. In contrast, the PWA-based device demonstrated a significantly improved T_{50} of approximately 38.68 hours, reflecting the higher intrinsic material stability of PWA. Remarkably, the device based on W07 not only demonstrated superior operational stability compared to PWA (T_{50} = 39.69 hours), but also delivered significantly enhanced EQE and luminance. These findings clearly demonstrate that the PWA–PMA solid-solution system achieves both high stability and superior performance, highlighting its potential as a highly effective hole injection layer.

We utilized conductive atomic force microscopy (C-AFM) measurements to compare the impact of ITO corrosion induced by PEDOT:PSS and PWA-PMA (W07). As shown in **Fig. S11**, three ITO glass substrates—bare, coated with PWA-PMA, and coated with PEDOT:PSS—were stored under an inert atmosphere for 7 days. Prior to C-AFM measurements, the HILs were completely removed by sequential cleaning with acetone and IPA. The ITO substrate previously coated with PEDOT:PSS exhibited the highest surface roughness (2.17 nm) and the lowest average current (0.258 nA) under a 0.1 V bias over a 10 × 10 μm² area, as shown in **Fig. S12**. In contrast, the ITO sample previously coated with PWA-PMA showed a significantly higher average current (0.627 nA), nearly three times greater than that of the PEDOT:PSS-treated sample, and even lower surface roughness (1.264 nm) compared to pristine ITO (1.4 nm). These results suggest that PWA-PMA causes substantially less corrosion to the ITO surface than PEDOT:PSS, which can be critical for preserving device performance and operational stability. This degradation in the PEDOT:PSS-treated sample may stem from the strong acidity of its components. While phosphotungstic acid hydrate (PWA) is known to have a pH around 2, PEDOT:PSS is reported to have an even lower pH (~1).

View Article Online
DOI: 10.1039/D5TC02166A

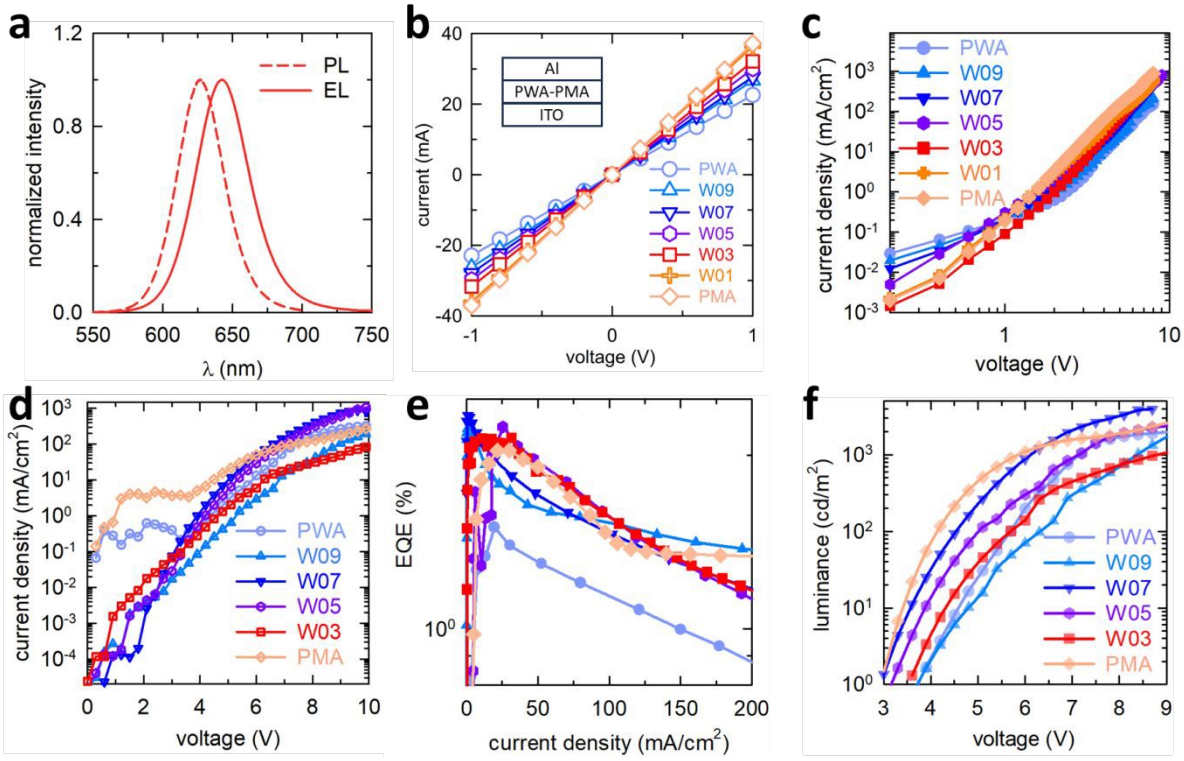

Fig. 4 (a) Normalized PL spectrum of the InP red QDs and an EL spectrum of the QLED using PWA-PMA as HIL. (b) current vs. voltage of ITO/PWA-PMA/Al. (c) current density vs. voltage of the HOD of PWA-PMA. Characteristics of QLED using PWA-PMA as HIL (d) current density vs. voltage, (e) EQE vs. current density, (f) luminance vs. voltage.

Table 1 Electrical properties of PWA-PMA thin films.

HIL	Conductivity [S/cm]	Mobility [cm^2/Vs]	Carrier concentration [$1/cm^3$]
PWA	4.59×10^{-5}	8.90×10^{-5}	3.22×10^{18}
W09	4.82×10^{-5}	1.02×10^{-4}	2.95×10^{18}
W07	5.20×10^{-5}	1.70×10^{-4}	1.91×10^{18}
W05	5.64×10^{-5}	2.42×10^{-4}	1.46×10^{18}
W03	6.86×10^{-5}	2.44×10^{-4}	1.76×10^{18}

View Article Online
DOI: 10.1039/D5TC02166A

W01	7.28×10^{-5}	3.97×10^{-4}	1.15×10^{18}
PMA	8.23×10^{-5}	5.96×10^{-3}	8.63×10^{16}

Table 2 QLED performance using PWA-PMA as HIL of QLED

HIL	EQE [%]	Turn-on V [V]	L_{max} [cd/m^2]	Current efficiency [cd/A]
PWA	1.50	3.9	1,956	1.67
W09	2.22	3.9	1,732	2.44
W07	2.34	3.0	3,952	2.50
W05	2.24	3.3	2,428	2.51
W03	2.14	3.6	1,057	2.42
W01	2.09	3.3	974	1.62
PMA	2.04	3.0	2,604	2.34

3. Experimental

3.1. Materials

Phosphotungstic acid hydrate and phosphomolybdic acid hydrate were purchased from Sigma-Aldrich. TFB (MW = 60,000) was purchased from OSM. Anhydrous ethanol (99.9%) was purchased from Daejung Chemicals & Metals Co. Ltd. Aluminum (99.999%) was purchased from ITASCO. All chemicals were used without any additional purification steps.

3.2. Preparation of PWA-PMA solid-solution hole injection layer

View Article Online
DOI: 10.1039/D5TC02166A

Film samples with the general formula $PW_{12-12x}Mo_{12x}O_{40}$ (x= 0, 0.1, 0.3, 0.5, 0.7, 0.9, and 1) were prepared *via* sol-gel method. The precursor solution (anhydrous ethanol in 20mg/mL) was prepared by dissolving phosphotungstic acid hydrate and phosphomolybdic acid hydrate based on the specified molar ratio. To fabricate the PWA HIL, spin-coating was employed at 3,000 rpm for 45 s, followed by preheating at 250°C for 30 min at ambient condition. (**Fig. S1**) (PWA: $PW_{12}O_{40}$, W09: $PW_{10.8}Mo_{1.2}O_{40}$, W07: $PW_{8.4}Mo_{3.6}O_{40}$, W05: $PW_6Mo_6O_{40}$, W03: $PW_{3.6}Mo_{8.4}O_{40}$, W01: $PW_{1.2}Mo_{10.8}O_{40}$, PMA: $PMo_{12}O_{40}$)

3.3. Fabrication of QLED

ITO substrates were sonicated in acetone and isopropyl alcohol for 30 min. It was then subjected to a cleaning process involving UV-ozone treatment for 15 min. Subsequently, PWA was spin-coated at 3,000 rpm for 45 s and annealed at 250°C for 30 min at ambient condition. A solution of TFB (8 mg/mL in chlorobenzene) was spin-coated at 3,000 rpm for 60 s and annealed at 160°C for 30 min at inert gas condition. Subsequently, red InP QDs (10 mg/mL) were spin-coated at 3,000 rpm for 20 s and annealed at 80°C for 30 min at inert gas condition. The ZnMgO NPs (in ethanol at a concentration of 25 mg/mL) were spin-coated at 3,000 rpm for 60 s at inert gas condition. Finally, the fabrication of the QLED was completed after thermal evaporation of a 100 nm-thick aluminum cathode.

3.4. Computational calculations

All solid-solution structures were generated using Special Quasi-random Structures (SQS) theory constructed with the Alloy Theoretic Automated Toolkit (ATAT).[24,25] We extracted a total energies of all atomic models performing DFT calculations by using Vienna Ab-initio Simulation Package (VASP).[26] The Perdew-Burke-Ernzerhof exchange-correlation functional was used to describe the exchange-correlation function.[27] During the structural optimization, the plane-wave energy cut off was set to 520 eV

View Article Online
DOI: 10.1039/D5TC02166A

to minimize Pulay stress. The Brillouin zone was sampled by using 100 k-points density per Å^{-1}of reciprocal lattice. To describe the Density of State (DOS), the gaussian smearing method was used for all alloy structures. All Gibbs free energies of mixing was computed by total energy extracted from DFT calculations. The Gibbs free energy of mixing is defined as

$$\Delta G_{mix}(x,T) = \Delta H_{mix}(x) - T\Delta S_{mix}(x)$$

where $\Delta H_{mix}(x)$ is the enthalpy of mixing as a function of composition x, T is a temperature, and $\Delta S_{mix}(x)$ is a entropy of mixing as a function of x. Here, the $\Delta H_{mix}(x)$ is defined as

$$\Delta H_{mix}(x) = E[P(Mo_{1-x}W_x)_{12}O_{40}] - (1-x)E[PMo_{12}O_{40}] - xE[PW_{12}O_{40}]$$

where x $E[P(Mo_{1-x}W_x)_{12}O_{40}]$ is the total energy of SQS structure, $E[PMo_{12}O_{40}]$, and E $[PW_{12}O_{40}]$ are the total energies of each $PMo_{12}O_{40}$ and $PW_{12}O_{40}$, respectively. The entropy of mixing is defined as

$$\Delta S_{mix}(x) = -nk_B[xln(x) + (1-x)\ln(1-x)\,]$$

where n is the cation site degeneracy, and k_B is a Boltzmann constant value of $8.617 \times 10^{-5} eV \cdot K^{-1}$.

3.5. Characterization

X-ray diffraction (XRD) was employed to assess the crystalline phase of the PWA-PMA solid-solution film using the SmartLab instrument by Rigaku. FTIR spectra were recorded in transmission mode by a Nicolet iS50 instrument by Thermo Fisher Scientific. Transmission electron microscopy (TEM) using a JEOL JEM 2100F instrument was employed to determine layer thickness and calculate lattice distances. Surface analysis of PWA-PMA solid-solution films was performed using a scanning electron microscope (SEM) (Nova NanoSEM 450, FEI).

View Article Online
DOI: 10.1039/D5TC02166A

AFM instrument from Park Systems (NX20) was utilized to study the surface morphologies and conductive properties of films. Ultraviolet photoelectron spectroscopy (UPS) was employed to evaluate the band levels of each layer using an XPS-theta probe machine from Thermo Fisher Scientific Co., equipped with a He1-photon source at 21.2 eV. UV–VIS spectra were acquired using a UV/VIS spectrophotometer (Cary-5000 instrument by Agilent). The current density–voltage–luminance (J–V–L) characteristics of the devices were measured using a spectroradiometer (CS-2000, Konica Minolta) with a Keithley 2400 source meter under ambient conditions.

4. Conclusions

A complete solid-solution range (x = 0–1) was achieved by combining PMA, which exhibits excellent charge transport properties despite its low stability, with PWA, which offers high stability but relatively less charge transport capabilities. Structural analysis confirmed the formation of the solid-solution and identified the range where phase transitions occur. Through computational method, an analysis of the partial density of states of PWA-PMA was conducted, identifying elements influencing the conduction and valence bands of the material. Additionally, an enhancement in carrier mobility and conductivity was observed in PWA as the molar ratio of Mo increased. In QLEDs, effective hole injection was achieved by adjusting the hole injection barrier in PWA-W05 and W03-PMA, which share the same crystal structure. Therefore, the results of our study could open the way to improving device efficiency and stability by exploring a new tunable HIL through solid-solutions.

Conflict of interest

View Article Online
DOI: 10.1039/D5TC02166A

The authors declare no conflict of interest.

Data availability

No primary research results, software or code have been included and no new data were generated or analyzed as part of this review.

Acknowledgements

This work was supported by Samsung Research Funding & Incubation Center of Samsung Electronics under Project Number SRFC-TC2103-04. This work was supported by the National Research Foundation of Korea(NRF) grant funded by the Korea government(MSIT) (RS-2024-00411892). Institute of Information & communications Technology Planning & Evaluation (IITP) grant funded by the Korea government(MSIT) (Grant No. 2020-0-01373, Artificial Intelligence Graduate School Program (Hanyang University)) and the research fund of Hanyang University (grant No. HY-202100000670049).

References

1 V. L. Colvin, M. C. Schlamp and A. P. Alivisatos, *Nature*, 1994, **370**, 354–357.

2 B. S. Mashford, M. Stevenson, Z. Popovic, C. Hamilton, Z. Zhou, C. Breen, J. Steckel, V. Bulovic, M. Bawendi and S. Coe-Sullivan, *Nat. photonics*, 2013, **7**, 407–412.

3 C. Y. Han and H. Yang, *J. Korean Ceram. Soc.*, 2017, **54**, 449–469.

4 H. Lee and J. Kim, *J. Korean Ceram. Soc.*, 2018, **55**, 174–177.

5 Y. H. Won, O. Cho, T. Kim, D. Y. Chung, T. Kim, H. Chung, H. Jang, J. Lee, D. Kim and E. Jang, *Nature*, 2019, **575**, 634–638.

View Article Online
DOI: 10.1039/D5TC02166A

6 H. Shen, Q. Gao, Y. Zhang, Y. Lin, Q. Lin, Z. Li, L. Chen, Z. Zeng, X. Li and Y. Jia, *Nat. Photonics*, 2019, **13**, 192–197.

7 X. Yang, E. Mutlugun, Y. Zhao, Y. Gao, K. S. Leck, Y. Ma, L. Ke, S. T. Tan, H. V. Demir and X. W. Sun, *Small*, 2014, **10**, 247–252.

8 J. M. Caruge, J. E. Halpert, V. Wood, V. Bulović and M. G. Bawendi, *Nat. photonics*, 2008, **2**, 247–250.

9 H. B. Cho, H. J. Kim, N. S. M. Viswanath, T. Samanta, J. W. Min, S. W. Jang, Y. M. Park, S. H. Jang, H. Yang and W. B. Im, *J. Mater. Chem. C*, 2024, **12**, 3196–3202.

10 H. B. Cho, J. Y. Han, H. J. Kim, N. S. M. Viswanath, Y. M. Park, J. W. Min, S. W. Jang, H. Yang and W. B. Im, *ACS Appl. Mater. Interfaces*, 2023, **15**, 29259–29266.

11 Q. Kang, Z. Zheng, Y. Zu, Q. Liao, P. Bi, S. Zhang, Y. Yang, B. Xu and J. Hou, *Joule*, 2021, **5**, 646–658.

12 M. Qu, Y. Li, P. Li, X. Yang, B. Wei and G. Chen, *Org. Electron.*, 2023, **120**, 106831.

13 S. Zhu, X. Gao, F. Dong, Y. Zhu, H. Zheng and Y. Li, *J. Catal.*, 2013, **306**, 155–163.

14 U. Filek, A. Bressel, B. Sulikowski and M. Hunger, *J. Phys. Chem. C*, 2008, **112**, 19470–19476.

15 F. Cao, Q. Wu, Y. Sui, S. Wang, Y. Dou, W. Hua, L. Kong, L. Wang, J. Zhang, T. Jiang and X. Yang, *Small*, 2021, **17**, 2100030.

16 F. Cao, Q. Wu and X. Yang, *ACS Appl. Mater. Interfaces*, 2019, **11**, 40267–40273.

17 X. López, J. J. Carbó, C. Bo and J. M. Poblet, *Chem. Soc. Rev.*, 2012, **41**, 7537–7571.

18 J. M. Maestre, X. Lopez, C. Bo, J. M. Poblet and N. Casañ-Pastor, *J. Am. Chem. Soc.*, 2001, **123**, 3749–3758.

19 L. Vegard, *Z. Physik*, 1921, **5**, 17–26.

20 A. R. Denton and N. W. Ashcroft, *Phys. Rev. A*, 1991, **43**, 3161–3164.

21 J. H. Hwang, E. Seo, S. Park, K. Lee, D. H. Kim, S. H. Lee, Y. W. Kwon, J. Roh, J. Lim and D. Lee, *Materials*, 2023, **16**, 1371.

22 W. K. Bae, Y.-S. Park, J. Lim, D. Lee, L. A. Padilha, H. McDaniel, I. Robel, C. Lee, J. M. Pietryga and V. I. Klimov, *Nat. comm.*, 2013, **4**, 2661.

23 F. Cai, H. Zong, M. Li, C. Li, G. Huang, J. Pascual, C. Liang, Z. Su, Z. Li, X. Gao, B. Hou, S. Wang, G. Zhou and Z. Du, *Nano Lett.*, 2024, **24**, 5284–5291.

24 A. Zunger, S. H. Wei, L. G. Ferreira and J. E. Bernard, *Phys. Rev. Lett.*, 1990, **65**, 353–356.

25 A. van de Walle, P. Tiwary, M. de Jong, D. L. Olmsted, M. Asta, A. Dick, D. Shin, Y. Wang, L. Q. Chen and Z. K. Liu, *Calphad*, 2013, **42**, 13–18.

26 G. Kresse and J. Furthmüller, *Phys. Rev. B*, 1996, **54**, 11169–11186.

27 J. P. Perdew, K. Burke and M. Ernzerhof, *Phys. Rev. Lett.*, 1996, **77**, 3865.

View Article Online
DOI: 10.1039/D5TC02166A

Data availability

The data supporting the findings of this study are available within the article and its ESI.